Nanoarchitectonics of Nanoporous Carbon Materials from *Achyranthus bidentata* (Datiwan) Stem for Supercapacitor Applications

Aabha Puri[1,2], Sabina Shahi[1,2], Chhabi Lal Gnawali[3], Katsuhiko Ariga[1,4], and Lok Kumar Shrestha[1,2]*

[1] *Research Center for Materials Nanoarchitectonics (MANA), National Institute for Materials Science (NIMS) (1-1 Namiki, Tsukuba, Ibaraki, 305-0044, JAPAN)*

[2] *Department of Materials Science, Institute of Pure and Applied Sciences, University of Tsukuba (1-1-1, Tennodai, Tsukuba, Ibaraki, 305-8573, JAPAN)*

[3] *Department of Applied Sciences and Chemical Engineering, Pulchowk Campus, Institute of Engineering (IOE), Tribhuvan University (Pulchowk, Lalitpur, 44700, NEPAL)*

[4] *Department of Advanced Materials Science, Graduate School of Frontier Sciences, The University of Tokyo (5-1-5 Kashiwanoha, Kashiwa, Chiba 277-8561, JAPAN)*

Running title: Biomass Nanoarchitectonics for Supercapacitor Applications

A. Puri, S. Shahi, C.L. Gnawali, K. Ariga and L.K. Shrestha

*Correspondence to: Lok Kumar Shrestha, Research Center for Materials Nanoarchitectonics (MANA), National Institute for Materials Science (NIMS), 1-1 Namiki, Tsukuba, Ibaraki, 305-0044, JAPAN

E-mail address: SHRESTHA.Lokkumar@nims.go.jp

Abstract:

Biomass is a sustainable carbon source to produce porous carbon materials. Due to the high surface area, tunable porosity, surface functionalities and high chemical stability, biomass carbons have extensively explored in sensing, separation, and energy storage and conversion applications. Here, we report on the fabrication of nanoporous activated carbon materials from a novel biomass precursor *Achyranthus bidentata* (Datiwan), using a low-energy method (carbonized at 500 °C). The effects of chemical activators (phosphoric acid (H_3PO_4), potassium hydroxide (KOH), and zinc chloride ($ZnCl_2$) on surface textural properties and energy storage capacity were systematically studied. The H_3PO_4 and $ZnCl_2$ activated samples (DAC-H500, DAC-Z500) exhibited the specific surface area of 724 and 758 $m^2\ g^{-1}$, respectively, and retained abundant surface oxygen functionalities, thereby leveraging decent specific capacitance of 201 F g^{-1} and 140 F g^{-1} at 1 A g^{-1} with 51% and 61.3% retention of their initial capacitance values at 10 A g^{-1}. The symmetric cell assembled with the DAC-Z500 delivered 3.5 Wh kg^{-1} energy density at a power density of 590 W kg^{-1} with good cycle life of 76% and 98% coulombic efficiency after 10,000 consecutive charge/discharge cycles. Datiwan, a self-grown, abundant biomass that is indirectly contributing to carbon emissions, is being utilized to prepare nanoporous carbon at a lower temperature, and it shows significant potential as an electrode material in energy storage applications.

Key words: *Achyranthus bidentata*, biomass, chemical activation, nanoporous carbon, supercapacitor

1 INTRODUCTION

Energy demand has been escalating due to rapid technological development, from which nearly 80% of energy comes from non-renewable fossil fuels, resulting in decreased availability and climate change, thereby necessitating a shift towards sustainable, renewable resources. Since renewable energy sources are intermittent, the development of efficient energy storage devices is crucial[1-4]. Energy storage devices are broadly classified as capacitors, supercapacitors (SCs), and rechargeable batteries. Although Li-ion batteries offer high energy density, supercapacitors have become indispensable due to their high specific power, rapid charging, long cycle life, and excellent rate performance. However, SCs are lagging behind batteries in terms of specific energy[5,6]. Intensive research has been carried out to improve supercapacitor's energy storage capacity by developing advanced electrode materials, selecting appropriate electrolytes, and expanding the operating voltage window[7]. The electrode material plays a crucial

role in enhancing the specific capacitance of supercapacitors. Primary materials such as activated carbons, transition metal oxides and their composites, conducting polymers, etc., have been well explored in supercapacitor applications[8-11]. Among these, biomass-derived activated carbons are found to be promising electrode materials due to their high surface area, well-developed hierarchical micro/mesoporosity, surface functionalities, and good electrical conductivity. Besides, they are the most abundant, cheap, and renewable resources[12,13]. Two main methods have been applied for the preparation of biomass-based activated carbons: physical activation (pyrolysis) and chemical activation[14,15]. Pyrolysis involves the thermal treatment of a precursor sample at very high temperatures. At the same time, the chemical method includes impregnation of chemical activating agents, such as zinc chloride, potassium hydroxide, phosphoric acid, sodium hydroxide, etc.[16], with the precursor like coconut fiber[17], Jackfruit seeds[18], rice husk[19], Lapsi seed stones[20], lotus seed[21], etc., for activation followed by carbonization. Chemical activation is preferred over pyrolysis, as it maximizes yield and surface area while providing well-controlled porosity by minimizing volatile products and tar formation, even at comparatively lower carbonization temperatures.

The activating agents play the pivotal role in the formation of pores and surface functionalities as they react differently with the components of biomass (cellulose, hemicellulose, lignin, and polysaccharides). Phosphoric acid (H_3PO_4) acts as a dehydrating agent and promotes cross-linking reactions in the bio-polymer matrix, resulting in mesopores and oxygen-containing groups that improve hydrophilicity and pseudo-capacitance. Zinc chloride ($ZnCl_2$) is a Lewis acid and also a strong dehydrating agent that promotes the formation of aromatic carbon sheets with a microporous structure. Similarly, potassium hydroxide (KOH) undergoes redox reactions with carbon, forming metallic K and various potassium compounds (K_2CO_3, K_2O), which intercalate and expand the carbon layers, yielding high-surface-area, electrically conductive carbon[22-27]. So far, many reports have described the synthesis of activated carbons using various activating agents and biomass precursors. For instance, the KOH-activated Horse gram seed-based carbon sample exhibited a high surface area of 2037 $m^2\ g^{-1}$, leveraging excellent specific capacitance of 396 F g^{-1} at 1 A g^{-1}, as reported by Adhikari and co-workers[28]. Similarly, Gnawali and co-workers[29] prepared a high surface area (1383 $m^2\ g^{-1}$) activated carbon from Harro seed stones by using $ZnCl_2$ as an activating agent and reported the specific capacitance of 329 F g^{-1} at 1 A g^{-1} current density.

Additionally, the *Eucommia ulmoides* Oliver-derived H_3PO_4-activated carbon sample prepared by Song and co-workers[30] showed a specific capacitance of 233 F g^{-1} at a current density of 0.2 A g^{-1}. These studies show the importance of biomass precursors, activating agents, and carbonization parameters in preparing a superior carbon-based electrode material with enhanced electrochemical performance by optimizing its surface textural properties. *Achyranthus bidentata* (Datiwan) is a medicinal plant belonging to the Amaranthaceae family, widely grown in tropical Asia, particularly in China, Japan, Korea, Nepal, and India. Datiwan is a self-grown plant that grows abundantly in the tropical jungles of Asian countries. It has not been utilized, contributing to carbon emissions and highlighting the detrimental impact on the environment. So, it is a sustainable, abundant, and economical precursor for the scalable production of porous carbon materials. Based on its chemical composition, Datiwan is a lignocellulosic material with high thermal stability, which is crucial for the preparation of a robust supercapacitor electrode material and for achieving a higher yield. On the other hand, it is composed of compounds such as triterpenoids, saponins, sterones, and alkaloids[31-33] that are rich in hydroxyl, carboxylic acid, anhydrides and esters as functional groups. These functional groups are the active sites of the biopolymers which decompose on thermal treatment releasing gases like CO, CO_2, and water vapors thereby creating pores into the carbon framework. Hence, Datiwan shows potential for the preparation of high-surface-area porous carbon materials. However, Datiwan has not been explored yet for the preparation of carbon materials for energy storage applications.

Herein, we report the fabrication of high surface area nanoporous carbon materials by the chemical activation of novel biomass precursor (*Achyranthus bidentata*) using three different activating agents, H_3PO_4, KOH, and $ZnCl_2$ at a lower carbonization temperature (500 °C). A significant increase in surface textural properties and retention of surface functionalities was observed. H_3PO_4- and $ZnCl_2$-activated samples exhibited high specific capacitance of 201 F g^{-1} and 140 F g^{-1}, respectively, in an aqueous electrolyte (1 M H_2SO_4). Furthermore, the assembled symmetrical supercapacitor cell delivered an energy density of 3.5 Wh kg^{-1} at a power density of 590 W kg^{-1} and excellent cycle life, with coulombic efficiencies of 76% and 98% after 10,000 cycles. These results demonstrate the enormous potential of Datiwan as a sustainable source of carbon material for electrochemical charge storage in supercapacitors.

2 EXPERIMENTAL PROCEDURES

2.1 Materials

The stems of Achyranthus bidentata (Datiwan) were purchased from the local market (Parbat, Nepal). Potassium hydroxide (KOH:

99.5%), zinc chloride ($ZnCl_2$: 98%), phosphoric acid (H_3PO_4: 85%), hydrochloric acid (HCl), and sulfuric acid (H_2SO_4: 1M) were purchased from Nacali Tesque Inc., Kyoto, Japan.

2.2. Preparation of nanoporous carbon materials

The stems of Datiwan were washed with distilled water, dried at 100 °C for 24 h, and then crushed to make a powder. The powder sieved to a 300-micrometer mesh was first heated in a muffle furnace at 300 °C for 3 h to remove moisture and volatile components from the biomass precursor, yielding a carbon-rich biochar. The obtained biochar was mixed separately with three different activating agents, phosphoric acid (H_3PO_4), potassium hydroxide (KOH), and zinc chloride ($ZnCl_2$) in a 1:1 ratio by wt. and mechanically mixed, ensuring their homogeneous distribution, and left for 24 h for activation. The mixture was then carbonized at 500 °C for 3 h under a nitrogen atmosphere at a flow rate of 120 cc min^{-1} in a tube furnace with a 10 °C min^{-1} temperature ramp. The samples obtained were then washed with 1M HCl solution and then with distilled water until neutral pH and dried at 80 °C for 12 h. The prepared activated carbon samples were referred to as DAC-H500, DAC-K500, and DAC-Z500, respectively. The biochar was carbonized in the absence of activating agents at a similar carbonization temperature and time to the reference sample and labelled as DP-500. The reactions that occur during carbonization with different activating agents are as follows:

$$nH_3PO_4 + C \rightarrow CH_n + 2P_nO_{3n+1} + (n-1)\,H_2O \quad (1)$$
$$2H_n + 2P_nO_{3n+1} \rightarrow P_4O_{10} + nH_2O \quad (2)$$
$$P_4O_{10} + 2C \rightarrow P_4O_6 + 2CO_2 \text{ or } CO\uparrow \quad (3)$$
$$P_4O_{10} \text{ or } P_4O_6 + CH \rightarrow PH_3\uparrow + CO_2 \text{ or } CO\uparrow \quad (4)$$

$$6KOH + 2C \rightarrow 2K_2CO_3 + 2K + 3H_2\uparrow \quad (5)$$
$$3KOH + (-O-CO) \rightarrow K_2CO_3 + K + H_2\uparrow + CO_2\uparrow \quad (6)$$
$$3KOH + (-C-OH) \rightarrow K_2CO_3 + K + H_2O + H_2\uparrow \quad (7)$$

2.3. Characterizations

The precursor powder and the prepared activated carbon samples were characterized by thermogravimetric analysis (TGA) using STA 2500 (Regulus, NETZSCH, Germany), attenuated total reflectance/Fourier-transform infrared (ATR/FTIR) spectroscopy using NICOLET iS20 (Thermo-Fischer Scientific, Waltham, MA, USA) and scanning electron microscopy (SEM) using S-4800 (Hitachi Co., Ltd. Tokyo, Japan) operated at 10 kV and 10 μA. Nitrogen adsorption/desorption isotherms of the carbon samples were characterized on an Autosorb-iQ2 instrument (Quantachrome, Boynton Beach, FL, USA) for the determination of the textural properties, including surface areas, pore volumes, and pore size distributions. Density functional theory (DFT) and the Barrett–Joyner–Halenda (BJH) model were used to obtain micropore and mesopore size distribution profiles, respectively.

2.4 Electrochemical measurements

2.4.1. Electrochemical measurements in a three-electrode cell

The analysis of the electrochemical properties of the prepared nanoporous carbon samples was performed in three-electrode cells using a CHI-660E electrochemical workstation, where the synthesized material, a platinum wire, and an Ag/AgCl electrode were used as working, counter, and reference electrodes, respectively, with 1 M H_2SO_4 as the electrolyte. For the fabrication of the working electrode, the synthesized carbon material/active material (80%) was mixed with carbon black (10%) for conductivity and PVDF (Polyvinylidene fluoride) (10%) as a binder for the active material. The slurry was made by mixing 2 mg of the prepared mixture with approximately 5 μL of NMP (N-methyl-2-pyrrolidone), which was then uniformly coated onto the 1 cm × 1 cm graphite sheet and dried overnight at 70 °C. The electrochemical performance of the electrode was evaluated using cyclic voltammetry (CV), galvanostatic charge-discharge (GCD), and electrochemical impedance spectroscopy (EIS). The specific capacitance (C_s) was calculated from the GCD curve using Eq. 8.

$$C_s = \frac{I \times \Delta t}{m \times \Delta V} \quad (8)$$

where I (A), Δt (s), m (g), and ΔV (V) are current, discharge time, mass of active electrode material, and operating voltage, respectively.

2.4.2. Electrochemical measurements in a two-electrode symmetric cell

The working electrode was prepared using the same protocol as mentioned in the three-electrode cell system. The electrochemical charge storage in the symmetric cell was analyzed using CV, GCD, and EIS. The specific capacitance of the electrode was calculated from GCD curves using Eq. 8. The energy density (E) and power density (P) of the supercapacitor were calculated using Eq. 9 and Eq. 10, respectively.

$$E = \frac{C_s \times \Delta V^2}{2 \times 3.6} \quad (9)$$

$$P = \frac{E \times 3600}{\Delta t} \quad (10)$$

where, C_s, ΔV and Δt are the specific capacitance (F g^{-1}), the operating voltage window (V) and the discharge time (s) respectively.

3 RESULTS AND DISCUSSION

3.1 Materials synthesis and characterization

Figure 1a shows the FTIR spectrum of Datiwan powder. The peak at ~ 3345 cm^{-1} in the precursor is due to the O–H stretching vibrations of alcoholic groups and moisture content in the precursor. The peak at 2928 m^{-1} corresponds to the C–H (str.) of the aliphatic group of cellulose. The peak at 1735 cm^{-1} is the typical signature of C=O in acetyl groups of ester and/or cellulose, hemicellulose, and lignin. The deformation of the O–H bonds of water molecules and the C–H bonds exhibited peaks at 1647 cm^{-1} and 1372 cm^{-1}, respectively. The peaks in the range 1000 cm^{-1} to 1200 cm^{-1} resemble the C–O stretching vibrations of cellulose and hemicellulose [28,34,35]. The thermal decomposition of Datiwan powder (**Fig.1b**) shows mass loss in three-steps, as observed in the TGA curve. The mass loss up to 200 °C in the first stage is due to the removal of moisture from the biomass. The gradual weight loss in the second stage (< 350 °C) resembles the decomposition of cellulose and hemicellulose. The third stage is due to the slow decomposition of lignin in a broad temperature range above 400 °C [36], which supports the conversion of biomass into porous carbon. Hence, the carbonization was performed at 500 °C.

The surface area, pore volume, and pore structure of the Datiwan-derived activated carbon samples were characterized using nitrogen adsorption-desorption isotherms. These samples exhibited mixed Type-I and Type-IV adsorption isotherms, indicating the presence of both micro- and mesopores[37]. The lower nitrogen uptake observed in the reference and the KOH-activated carbon samples can be attributed to their lack of porosity. However, the samples activated with phosphoric acid and zinc chloride exhibited a significant amount of nitrogen adsorption at low relative pressure ($P/P_0 = 0.1$), suggesting the presence of micropores. The plateaus at higher pressures, along with the hysteresis loop, were indicative of capillary condensation occurring in the mesopores. DFT and BJH models were used to analyze the mesopore and micropore size distributions, respectively, which showed the prominent peaks confirming the formation of hierarchical micro- and mesoporous carbon architectures. The surface textural properties of these samples are illustrated in (**Table 1**). It highlights the impact of activating agents on surface textural properties at 500 °C. Both DAC-H500 and DAC-Z500 possess increased surface area and suitable pore-size distributions (2-5 nm) for energy storage in supercapacitors. The surface area of the sample DAC-K500 is the lowest among the activated carbon samples. This may be due to the inadequate temperature needed for the reduction of KOH into the metallic potassium (>762 °C), a process that facilitates pore formation by intercalating into the carbon lattice.

Figure 2 displays the scanning electron microscopy (SEM) images of the as-prepared nanoporous carbon materials alongside the counter sample. At low resolution, the surface morphology of the resulting activated carbon samples (DAC-H500, DAC-K500, DAC-Z500) and the reference sample (DP-500) revealed large macroporous channels with honeycomb-like architectures. The abundant macroporous morphology observed in the DAC-K500 can be attributed to the synergetic effect of strong alkaline etching and the presence of saponins in the biomass, which promote extensive gas evolution and pore expansion during carbonization. In contrast, zinc chloride and phosphoric acid primarily act as dehydrating and crosslinking agents, resulting in a compact carbon framework dominated by micro- and mesopores. At higher magnification, uniformly distributed mesoporous channels are observed in phosphoric acid- and zinc chloride-activated samples DAC-H500 and DAC-Z00, respectively. However, the reference sample lacks mesopores, as evidenced by the solid surface at higher resolution, underscoring the importance of chemical activation in the formation of porous architectures. The presence of abundant macro- and mesoporous structures in chemically activated carbon samples is beneficial, as it provides pathways for electrolyte ions to diffuse into the electrode material, thereby enhancing charge

storage capacity.

The FTIR spectra (**Fig. 3a**) of the resulting carbon samples show peaks at 1050, 1396, 1580, and 3348 cm^{-1}, which correspond to C–O–C stretching vibrations in anhydrides, O–H bending in carboxylic acids, C=C stretching in alkenes, and O–H stretching, respectively. The significant peak at 1150 cm^{-1} in the sample DAC-H500 is due to C–O stretching, indicating the presence of surface oxygen functionalities[38,39]. The Raman spectra (**Fig. 3b**) of the prepared carbon materials contain two prominent bands at 1360 and 1593 cm^{-1} corresponding to the *D* (presence of defects) and *G* (degree of pure graphite) bands of sp2-bonded carbon atoms, respectively. In carbon materials, the *D*-band corresponds to the A_{1g} symmetrical mode of vibration with respect to the inversion center, and the *G*-band corresponds to stretching vibrations with E_{2g} symmetry. The intensity ratio of *D* and *G*-bands (I_D/I_G) gives information about the structural disorder of the material[40,41]. The I_D/I_G values of the samples DP-500, DAC-H500, DAC-K500, and DAC-Z500 are 0.77, 0.81, 0.77, and 0.75, respectively. The optimal intensity ratio of the phosphoric acid-activated carbon sample indicates a greater number of defects in the material, leveraging an elevated number of active sites that are crucial to enhancing the electrochemical performance of the electrode material in supercapacitors.

3.2 Electrochemical performance in a three-electrode system

Figure 4a is the comparative CV profile of reference and activated samples at a fixed scan rate of 5 mV s^{-1}. All the samples exhibit a quasi-rectangular shape in the CV profiles, resembling the electrical double-layer charge (EDLC) storage mechanism[42-45]. The redox peaks at around 0.5 V (oxidation) and 0.4 V (reduction) are due to the surface functionalities (oxygen). The current collection of DAC-H500 and DAC-Z500 is higher, which can be explained based on their higher surface areas, large porosities, and well-defined micro- and mesopore size distributions. Despite the higher specific surface area of the DAC-Z500 sample, the current collection of DAC-H500 is slightly greater, which is attributed to the well-coordination of the micro- and mesopore distribution for efficient electrolyte ion transport, along with the increase in the number of defects, leveraging enhanced pseudocapacitive behavior of the material that is in agreement with the FTIR and Raman results. The integral current collection of the DP-500 and DAC-K500 is due to their lack of porosity, indicating poor charge storage capacity. The CV profiles recorded at different scan rates (5- 100 mV s^{-1}) sustain a quasi-rectangular shape (**Fig. 4b – d**), suggesting fast electrolyte ion diffusion to the electrode surface due to the presence of a hierarchy of micro- and mesopores.

Figure 5a compares the GCD profiles of the as-prepared samples at the fixed current density of 1 A g^{-1}. The triangular shape of the charge-discharge curve, along with the linear discharge decay, indicates EDLC behavior[46,47]. The sample DAC-H500, with well-coordinated synergetic surface textural properties and surface functionalities (defects), exhibits the longest discharge time, leveraging the optimal energy storage capacity of the electrode. The specific capacitance values of DP-500 and DAC-K500 are 38 F g^{-1} and 42 F g^{-1}, respectively. Their lower capacitance values can be attributed to the lack of porosity and lower surface area. However, DAC-H500 and DAC-Z500 exhibit higher capacitances of 201 F g^{-1} and 140 F g^{-1}, respectively. The increase in the capacitance of these two samples can be explained by their elevated surface textural properties. The optimal capacitance of DAC-H500 is due to effective electrolyte infiltration through the elevated mesopores of the high-surface-area carbon sample, along with the abundance of oxygen functionalities at the surface (evident by the increase in the I_D/I_G ratio in the Raman and FTIR spectra), which contribute to the pseudo-capacitance. The retention of the quasi-triangular shape of the GCD curve (**Fig. 5b – c**) even at higher current density suggests fast electrolyte ion transport to the electrode surface. The C_s versus current density plot (**Fig. 5d-e**) shows that the sample DAC-H500 exhibited a capacitance retention of 102 F g^{-1} at 10 A g^{-1} (50.7%). The sample DAC-Z500 retained 61.3% of the initial capacitance at a current density of 10 A g^{-1}, demonstrating better rate performance. The Nyquist plot (**Fig. 5f**) was used to analyze the charge-storage mechanism and the associated resistance. In the low-frequency region, all samples showed straight lines inclined at ~45°, indicating Warburg impedance resembling pseudocapacitive behavior due to oxygen as surface functionalities[48,49]. The equivalent series resistance (ESR) of DAC-H500 and DAC-Z500 is obtained from the intersection point on the real impedance axis as 0.58 Ω and 0.47 Ω, respectively, indicating good electrical conductivity of the Datiwan-derived activated carbon materials. The slightly lower ESR of DAC-Z500 compared to DAC-H500 has contributed to better rate performance. The surface-based and diffusion-based charge storage contribution was calculated from the CV profiles using Eq. (11)[50-52].

$$i = av^b \quad (11)$$

where, '*a*' and '*b*' are constants, *i* (A g^{-1}) is the peak current, and *v* (mV s^{-1}) is the scan rate.

Figure 5g shows the log(*v*) vs. log(*i*) plot of two optimal samples. The *b*-value of DAC-H500 and DAC-Z500 are 0.76 and 0.79, respectively, inferring the well-coordinated surface and diffusion-driven charge storage mechanisms. **Figure 5h** further displays the capacitance contribution by these two mechanisms. About 72% charge contribution at 5 mV s^{-1} in the sample DAC-H500 is by the

diffusion-controlled mechanism, while the surface-controlled mechanism contributed about 28% charge. Nevertheless, the surface-controlled capacitive current contribution gradually increased at higher scan rates from 28% to 64%.

3.3. Electrochemical performance in a symmetrical cell

The symmetric cell was constructed with the material having optimal surface textural properties (DAC-Z500), and the electrochemical performance was measured at an operating voltage of 1.2 V in an aqueous electrolyte (1M H_2SO_4). The quasi-rectangular shape of the CV curve (**Fig. 6a**) indicates capacitive behavior of the cell, and the retention of this shape at higher scan rates suggests fast charge-transfer kinetics. The EDLC behavior is further supported by the triangular curves in GCD profiles (**Fig. 6b**). The specific capacitance of 18 F g^{-1} at 1 A g^{-1} was obtained from the GCD plot. The C_s versus current density plot (**Fig. 6c**) shows around 38% capacitance retention at a current density of 5 A g^{-1}. **Figure 6d** shows the Nyquist plot before and after the cycle test. No significant variation is observed in the plots, indicating that the electrode-electrolyte interface is not altered by the cycles, resulting in extended cycle stability[53, 54]. The cyclic stability (**Fig. 6e**) measured at 5 A g^{-1} shows comparable cyclic performance with 76% capacitance retention and 98% coulombic efficiency even after 10,000 consecutive charge/discharge cycles, which are crucial for the longevity of the supercapacitor device. The Ragone plot compares the energy density of the supercapacitor device, leveraging certain power density[55, 56], and is represented in **Figure 6f**. DAC-Z500 delivered a energy density of 3.5 Wh kg^{-1} at a power density of 590 W kg^{-1}, which is better and/ or comparable to the reported biomass-derived activated carbon, considering the energy consumption for the preparation of the nanoporous carbon material. The reports show that the activated carbon prepared from Sichuan pepper delivered 4.2 Wh kg^{-1} at 250 W kg^{-1} power density [57]. Similarly, the carbon obtained from chitin saccharide exhibited 3.5 Wh kg^{-1} at 5000 W kg^{-1} [58], *Shorea robusta*-derived carbon showed 3 Wh kg^{-1} at 99.6 W kg^{-1} [59], and Barro seed stone-derived carbon delivered 7.1 Wh kg^{-1} at 600 W kg^{-1} power density[60]. These results demonstrate that the Datiwan-derived activated carbon has the potential as an electrode material for supercapacitor devices.

4 CONCLUSION

In summary, this work demonstrates that *Achyranthus bidentata* (Datiwan) is an effective and previously unexplored biomass precursor for producing hierarchical nanoporous carbon at relatively low carbonization temperature. The comparative activation study clearly shows that the nature of chemical activating agents strongly governs pore development and surface chemistry, thereby affecting the electrochemical performance in supercapacitors. For this specific biomass, acidic and neutral activators promoted the formation of micro-mesoporous networks and oxygen-rich surfaces, which are favorable for ion transport and pseudocapacitive charge storage, whereas differences in activation chemistry led to distinct surface textural and electrochemical responses. Among the prepared samples, the $ZnCl_2$-activated sample exhibited a balanced combination of porosity, surface functionality, graphitization, and structural stability, enabling reliable performance in a symmetrical supercapacitor configuration with acceptable energy delivery and long-term cycling stability. The observed electrochemical behavior highlights the importance of hierarchical porosity and surface oxygen functionalities for efficient charge storage even at lower carbonization temperatures. Overall, this study indicates Datiwan as a sustainable, low-cost, scalable carbon source for energy storage applications, while also providing insight into how activation chemistry can be tailored to optimize the performance of the electrode material in supercapacitors.

ACKNOWLEDGMENT

AP is thankful to the National Institute of Materials Science (NIMS), Tsukuba, Japan, for the NIMS Junior Fellowship for the Ph.D. program. SS is thankful to the Ministry of Education, Culture, Sports, Science and Technology (MEXT) for the Ph.D. program. This work was partially supported by Japan Society for the Promotion of Science KAKENHI Grant Numbers, JP23H05459 and JP25H00898.

References

1) Lakshmi, K.C.S.; Vedhanarayanan, B. High-Performance Supercapacitors: A Comprehensive Review on Paradigm Shift of Conventional Energy Storage. *Batteries* **9** (4), 202 (2023).

2) Shrestha, L.K.; Ariga, K.; Nanoarchitectonics for Supercapacitor: Biomass vs. Fullerene. *Front. Batter. Electrochem.* ***3***, 1422400 (2024).

3) Simon, P.; Gogotsi, Y. Materials for Electrochemical Capacitors. *Nature Mater.* **7**, 845-854 (2008).

4) Simon, P.; Gogotsi, Y. Perspectives for Electrochemical Capacitors and Related Devices. *Nature Mater.* **19**, 1151-1163 (2020).
5) Dissanayake, K.; Abeywardana, D.K. A Review of Supercapacitors: Materials, Technology, Challenges, and Renewable Energy Applications. *J. Energy* Storage **96**, (2024).
6) Shuja, A.; Khan, H.R.; Murtaza, I.; Ashraf, S.; Abid, Y.; Farid, F.; Sajid, F. Supercapacitors for Energy Storage Applications: Materials, Devices and Future Directions: A Comprehensive Review. *J. Alloys Compd.* **1009**, 176924 (2024).
7) Pal, B.; Yang, S.; Ramesh, S.; Thangadurai, V.; Jose, R. Electrolyte Selection for Supercapacitive Devices: A Critical Review. *Nanoscale Adv.* **1**, 3807–3835 (2019).
8) Yuksel, R.; Karakehya, N. High Energy Density Biomass-Derived Activated Carbon Materials for Sustainable Energy Storage. *Carbon* **221,** 118934 (2024).
9) An, C.; Zhang, Y.; Guo, H.; Wang, Y.; Metal Oxide-Based Supercapacitors: Progress and Prospectives. *Nanoscale Adv.* **1**, 4644 (2019).
10) Iqbal, Md. F.; Nasir, F.; Shabbir, F.; Babar, Z.U.D.; Saleem, Md. F.; Ullah, K.; Sun, N.; Ali, F. Supercapacitors: An Emerging Energy Storage System. *Adv. Energ. Sust. Res*. **6**, 2400412 (2025).
11) Moussa, M.; El-Kady, M.F.; Dubal, D.; Tung, T.T.; Nine, Md. J.; Mohamed, N.; Kaner, R.B.; Losic, D. Self-Assembly and Cross-Linking of Conducting Polymers into 3D Hydrogel Electrodes for Supercapacitor Applications. *ACS Appl. Energy Mater.* **3**, 923-932 (2020).
12) Shrestha, L.K.; Shahi, S.; Gnawali, C.L.; Adhikari, M.P., Rajbhandari, R.; Pokharel, B.P.; Ma, R.; Shrestha, R.G.; Ariga, K. *Phyllanthus emblica* Seed-Derived Hierarchically Porous Carbon Materials for High-Performance Supercapacitor Applications. *Materials* **15**, 8335 (2022).
13) Chaudhary, R.; Maji, S.; Shrestha, R.G.; Shrestha, R.L.; Shrestha, T.; Ariga, K.; Shrestha, L.K. Jackfruit Seed-Derived Nanoporous Carbons as the Electrode Material for Supercapacitors. *Carbon* **6**, 73 (2020).
14) Heidarinejad, Z.; Dehghani, M.H.; Heidari, M.; Javedan, G.; Ali, I.; Sillanpaa, M. Methods for Preparation and Activation of Activated Carbon: A Review. *Env. Chem. Lett.* **18**, 393-415 (2020).
15) Feng, P.; Li, J.; Wang, H.; Xu, Z. Biomass-Based Activated Carbon and Activators: Preparation of Activated Carbon from Corncob by Chemical Activation with Biomass Pyrolysis Liquids. *ACS Omega* **5**, 24064-24072 (2020).
16) Din, I. Md.; S. Ashraf, S.; Intisar, A. Comparative Study of Different Activation Treatments for the Preparation of Activated Carbon: A Mini-Review. *Sci. Prog.* **100**(3), 299-312 (2017).
17) Hamid, M.; Dayana, I.; Satria, H.; Ramdan, D.; Siregar, F. Md.; Sholeha, D.; Marbun, J.; Wijoyo, H.; Porous Hard Carbon Derived from Coconut Biomass Waste as Electrode Material for Supercapacitor. *J. Colloid Interface Sci.* **19,** 10047 (2025).
18) Maji, S.; Chaudhary, R.; Shrestha, R.G.; Shrestha, R.L.; Demir, B.; Searles, D.J.; Hill, J.P.; Yamauchi, Y.; Ariga, K.; Shrestha, L.K. High-Performance Supercapacitor Materials Based on Hierarchically Porous Carbons Derived from *Artocarpus heterophyllus* Seed. *ACS Appl. Energy Mater.* **4**, 12257-12266 (2021).
19) Shrestha, L.K.; Thapa, M.; Maji, S.; Shrestha, R.G.; Pradhananga, R.R.; Ariga, K. Rice Husk-Derived High Surface Area Nanoporous Carbon Materials with Excellent Iodine and Methylene Blue Adsorption Properties. *Carbon* **5**, 10 (2019).
20) Shrestha, L.K.; Rajbhandari, R.; Pokharel, B.P.; Shrestha, R.G.; Ariga, K.; S. Maji, B.P. Pokharel, R. Rajbhandari, Shrestha, R.L.; Pradhananga, R.R.; Hill, J.P. High Surface Area Nanoporous Graphitic Carbon Materials Derived from Lapsi Seed with Enhanced Supercapacitance. *Nanomaterials* **10**, 728 (2020).
21) Shrestha, L.K.; Chaudhary, R.; Shrestha, R.G.; Ariga, K.; Maji, S.; Hill, J.P.; Shrestha, T.; Tamrakar, B.M. Nanoarchitectonics of Lotus Seed Derived Nanoporous Carbon Materials for Supercapacitor Applications. *Materials* **13**, 54342 (2020).
22) Joshi, S.; Shrestha, R.G.; Pradhananga, R.R.; Ariga, K.; Shrestha, L.K. High Surface Area Nanoporous Activated Carbons Materials from *Areca catechu* Nut with Excellent Iodine and Methylene Blue Adsorption. *Carbon* **8**, 2 (2022**).**
23) Togibasa, O.; Mumfaijah, M.; Allo, Y.K.; Dahlan, K.; Ansanay, Y.O. The Effect of Chemical Activating Agent on the Properties of Activated Carbon from Sago Waste. *Appl. Sci*. **11**, 11640 (2021).
24) Gao, Y.; Yue, Q.; Gao, B.; Li, A. Insight into Activated Carbon from Different Kinds of Chemical Activating Agents: A Review. *Sci. Total Env.* **746,** 141094 (2020).
25) Hupian, M.; Galambos, M.; Viglasova, E.; Rosskopfova, O.; Kusumkar, V.V.; Dano, M. Activated Carbon Treated with Different Chemical Agents for Pertechnetate Adsorption. *J. Radioanal. Nucl. Chem.* **33**, 31815–1829 (2024).
26) Liu, P.; Sun, S.; Huang, S.; Wu, Y.; Li, X.; Wei, X.; Wu, S. KOH Activation Mechanism in the Preparation of Brewer's Spent Grain-Based Activated Carbons. *Catalysts* **14**, 814 (2024).
27) Akl, M.A.; Mostafa, A.G.; Al-Awadhi, M.; Al-Harwi, W.S.; El-Zeny, A.S. Zinc Chloride Activated Carbon Derived from Date Pits for Efficient Biosorption of Brilliant Green: Adsorption Characteristics and Mechanism Study. *App. Water Sci.* **13**, 226 (2023).
28) Adhikari, M.P.; Shahi, S.; Ma, R.; Hill, J.P.; Ariga, K.; Shrestha, L.K. Ultrahigh Surface Area Self-Nitrogen-Doped Nanoporous Carbon Materials from *Macrotyloma uniflorum* (Horse Gram) Seed for High-Performance Supercapacitor Applications. *J. Power Sources* **631,** 236239 (2025).
29) Gnawali, C.L.; Shrestha, L.K.; Hill, J.P.; Ma, R.; Ariga, K.; Adhikari, M.P.; Rajbhandari, R.; Pokharel, B.P.; Nanoporous Activated Carbon Material from

Terminalia chebula Seed for Supercapacitor Application. *Carbon* **9**, 109 (2023).
30) Song, H.; Qu, Q.; Yang, Z.; Zhang, Y.; Qiu, L.; Zhao, Y.; Li, C.; Zhu, M.; Yang, X.; Supercapacitor Performance of Activated Carbon from *Eucommia Ulmoides* Oliver Wood Optimized by the Activation Method. *ACS Omega* **10**, 15368-15380 (2025).
31) Rahman, N.F.; Sharma, K.; Laskar, S.; Ali, S.; Ahmed, A. Md.; Terang, W.; Meitei, N.D.; Khan, H.; Ahamad, I.Md.; Bharadwa, R.; Formulation and Evaluation of *Achyranthes bidentata* Root Extract Based Herbal-insecticide. *J. Natrl. Remeds.* **24**, 2320-3358 (2024).
32) Chen, Y.R.; Niu, Y.S.; Zhou, H.L. *Achyranthes bidentata* Blume (Amaranthaceae): A Review of its Botany, Traditional Uses, Phytochemistry, Pharmacology, and Toxicology. *J. Pharm. Pharmacol.* **76**, 930-966 (2024).
33) Yu, J.; Wang, X.; Botirov, E.Kh.; Dong, H.; Gusakova, S.D.; Liu, W. Chemical Constituents from *Achyranthes bidentata* and their Antihyperuricemic Acid Activities. *Chem. Nat. Compd.* **61**, 52-55, (2025).
34) Hoang, T.D.; Liu, Y.; Le, M.T. Synthesis and Characterization of Biochars and Activated Carbons Derived from Various Biomasses. *Sustainability* **16**, 5495 (2024).
35) Varol, E.A.; Mutlu, U. TGA-FTIR Analysis of Biomass Samples Based on the Thermal Decomposition Behavior of Hemicellulose, Cellulose, and Lignin. *Energies* **16** (2023).
36) Kundu, C.; Biswas, S.; Thomas, B.S.; Appadoo, D.; Duan, A.; Bhattacharya, S. Evolution of Functional Group of Lignocellulosic Biomass and its Delignified form During Thermal Conversion Using Synchrotron-based THz and Laboratory-based In-situ DRIFT Spectroscopy. *Fuel* **348**, 128579 (2023).
37) Brandao, A.T.S.C.; State, S.; Costa, R.; Potorac, P.; Vazquez, J.A.; Valcarcel, J.; Silva, A.F.; Anicai, L.; Enachescu, M.; Pereira, C.M. Renewable Carbon Materials as Electrodes for High-Performance Supercapacitors: From Marine Biowaste to High Specific Surface Area Porous Biocarbons. *ACS Omega* **8**, 18782-18798 (2023).
38) Siipola, V.; Tamminen, T.; Kalli, A., Lahti, R., Romar, H., Rasa, K.; Keskinen, R.; Hyvaluoma, J.; Hannul, M.; Wikberg, H. Effects of Biomass Type, Carbonization Process, and Activation Method on the Properties of Bio-Based Activated Carbons. *Bioresources* **13**(3), 5976-6002 (2018).
39) Raheel, F.; Rafay, A.; Bibi, B.; Ahmad, S.; Ali, Z.; Saleem, M.; Butt, M.S.; Rehman, A.U.; Irfan, M. Synthesis and Characterization of Activated Carbon and Its Application for Wastewater Treatment. *Mater. Proc.* **17**, 4 (2024).
40) Ghosh, S.; Santhosh, R.; Jeniffer, S.; Raghavan, V.; Jacob, G.; Nanaji, K.; Kollu, P.; Jeong, S.K.; Grace, A.N. Natural Biomass Derived Hard Carbon and Activated Carbons as Electrochemical Supercapacitor Electrodes. *Sci. Rep.* **9**,16315 (2019).
41) Minakshi, M.; Mujeeb, A.; Whale, J.; Evans, R.; Aughterson, R.; Shinde, P.A.; Ariga, K.; Shrestha, L.K. Synthesis of Porous Carbon Honeycomb Structures Derived from Hemp for Hybrid Supercapacitors with Improved Electrochemistry. *ChemPlusChem* **89**, e202400408 (2024).
42) Shrestha, R.G.; Maji, S.; Mallick, A.K.; Jha, A.; Shrestha, R.M.; Rajbhandari, R.; Hill, J.P.; Ariga, K.; Shrestha, L.K. Hierarchically Porous Carbon Materials from Phoenix Dactylifera Seed for High-Performance Supercapacitor Applications. *Bull. Chem. Soc. Jpn*. ***95***, 1060-1067(2022).
43) Shrestha, R.G.; Shrestha, L.K.; Ariga, K. Carbon Nanoarchitectonics for Energy and Related Applications. *C –J. Carbon Res.* **7**, 73 (2021).
44) Kalam, N.A.; Sengottaiyan, C.; Jayavel, R.; Ariga, K.; Shrestha, R.G.; Subramani, T.; Sankar, S.; Shrestha, L.K. Vanadium Sulfide/Reduced Graphene Oxide Composite with Enhanced Supercapacitance Performance. *J. Taiwan Inst. Chem. Eng.* ***92***, 72-79 (2018).
45) Gnawali, C.L.; Shahi, S.; Manandhar, S.; Shrestha, G.K.; Adhikari, M.P.; Rajbhandari, R.; Pokharel, B.P. Porous Activated Carbon Materials from Triphala Seed Stones for High-performance Supercapacitor Applications. *BIBECHANA* **20**, 10-20 (2023).
46) Arsha, M.S.; Biju, V. A 3.5 V Supercapacitor with Ultrahigh Energy and Power Capabilities using Thermally Deoxygenated Graphite Oxide Electrodes and Water-in-Salt Electrolyte. *Energy Fuels* **38**, 19076-19087 (2024).
47) Shao, Y.; El-Kady, M.F.; Sun, J.; Li, Y.; Zhang, Q.; Zhu, M.; Wang, H.; Dunn, B.; Kaner, R.B. Design and Mechanisms of Asymmetric Supercapacitors. *Chem. Rev*. **118**, 9233-9280 (2018).
48) Lazanas, A.Ch.; Prodromidis, M.I. Electrochemical Impedance Spectroscopy -A Tutorial. *ACS Meas. Sci. Au* **3**, 162-193(2023).
49) Qu, D.; Wang, G.; Kafle, J.; Harris, J.; Crain, L.; Jin, Z.; Zheng, D. Electrochemical Impedance and its Applications in Energy-Storage Systems. *Small Methods* **2**, 1700342 (2018).
50) Patil, R.; Pradhan, L.; Matsagar, B.M.; Agrawal, O.; Wu, W.; Jena, B.K.; Dutta, S. High-Performance Asymmetric Supercapacitor Device with Nickel–Cobalt Bimetallic Sites Encapsulated in Multilayered Nanotubes. *Energy Adv.* **2**, 1650-1659 (2023).
51) Ali, E. Surface Diffusion and Adsorption in Supercapacitors. *ACS Sustain. Chem. Eng*. **7**, 3692-3701(2019).
52) Mansi, Dubey, P.; Shrivastav, V.; Hołdy´nski, M.; Sundriyal, S.; Tiwari, U.K.; Deep A. Unraveling the Surface-Diffusion Charge Contribution Studies of Zeolitic-Imidazolate-Frameworks-Based Core–Shell Structure for High-Performance Hybrid Supercapacitors. *Energy Technol.* **12**, 2400722 (2024).
53) Wang, Q.; Yan, J.; Wang, Y.; Wei, T.; Zhang, M.; Jing, X.; Fan Z. Three-dimensional Flower-like and Hierarchical Porous Carbon Materials as High-rate Performance Electrodes for Supercapacitors. *Carbon* **67**, 119-127 (2014).
54) Mei, B.A.; Munteshari, O.; Lau, J.; Dunn, B.; Pilon L. Physical Interpretations of Nyquist Plots for EDLC Electrodes and Devices. *J. Phys. Chem. C* **122**, 194-206 (2018).
55) Lee, S.C.; Jung W.Y. Analogical Understanding of the Ragone Plot and a New Categorization of Energy Devices. *Energy Procedia* **88,** 526-530 (2016).

56) Allagui, A.; Fouda, E.Md.; Elwakil, A.S. Communication - The Ragone Plot of Supercapacitors Under Different Loading Conditions. *J. Electrochem. Soc.* **167**, 020533 (2020).
57) Zhang, H.; Xiao, W.; Zhou, W.; Chen, S.; Zhang, Y. Hierarchical Porous Carbon Derived from Sichuan Pepper for High-Performance Symmetric Supercapacitor with Decent Rate Capability and Cycling Stability. *Nanomaterials* **9**, 553 (2019).
58) Shrestha, D.; Rajbhandari, A. The Effects of Different Activating Agents on the Physical and Electrochemical Properties of Activated Carbon Electrodes Fabricated from Wood-Dust of *Shorea robusta. Heliyon* **7**, e07917 (2021).
59) Deshpande, A.; Rawat, S.; Patil, I. M.; Rane, S.; Bhaskar, T.; Ogale, S.B.; Hotha, S. Converting Renewable Saccharides to Heteroatom Doped Porous Carbons as Supercapacitor Electrodes. *Carbon* **214**, 118368 (2023).
60) Manandhar, S.; Gnawali, C.L.; Rajbhandari, R.; Ma, R.; Hill, J.P.; Ariga, K.; Shrestha, L.K. Enhanced Supercapacitance Performance of Hierarchically Porous Carbon Obtained from *Terminalia bellirica* (Barro) Seed Stone. *ACS Appl. Energy Mater.* **8**, 8100-8109 (2025).

Legends of Figures:

Fig. 1 (a) FTIR spectrum of Datiwan powder, (b) TGA curve of Datiwan powder, (c) Nitrogen sorption isotherms of reference and the activated carbon samples, and (d) the corresponding pore size distribution obtained by DFT-method. The closed and open symbols in Panel (c) represents adsorption and desorption of nitrogen gas, respectively.
Fig. 2 SEM images of as-prepared carbon materials. (a-c) DP-500, (d-f) DAC-H500, (g-i) DAC-K500 and (j-l) DAC-Z500.
Fig. 3 (a) FTIR and (b) Raman scattering spectra of DP-500, DAC-H500, DAC-K500, and DAC-Z500.
Fig. 4 (a) CV curves at a scan rate of 5 mV s^{-1}, (b) CV profile of DP-500 (reference sample) at different scan rates (5 to 100 mV s^{-1}), (c) CV curves of DAC-H500 at different scan rates (5 to 100 mV s^{-1}), (d) CV curves of DAC-Z500 at different scan rates (5 to 100 mV s^{-1}).
Fig. 5 Electrochemical performance in a three-electrode cell. (a) Comparative GCD plot at a current density of 1 A g^{-1}, (b) and (c) GCD plots of optimal samples at different current density (1 to 20 A g^{-1}), (d) and (e) Comparative plots of C_s vs. current density (1 to 20 A g^{-1}), (f) Nyquist plot, (g) linear plot of logi vs. logυ, and (h) Current contribution in DAC-H500.
Fig. 6 Electrochemical performance of DAC-Z500 in a symmetric two-electrode cell. (a) CV plots at different scan rates (5 to 100 mV s^{-1}), (b) GCD at different current densities (1 to 10 A g^{-1}), (c) C_s vs. current density plot, (d) Nyquist plot before and after cycle test, (e) cyclic performance, and (f) Ragone plot.

〔**Figure**〕 :

Fig. 1 (sheet 1)

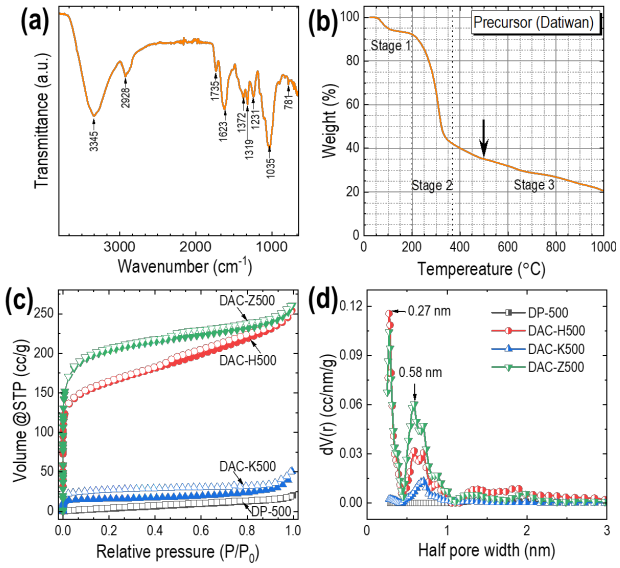

Fig. 2 (sheet 2)

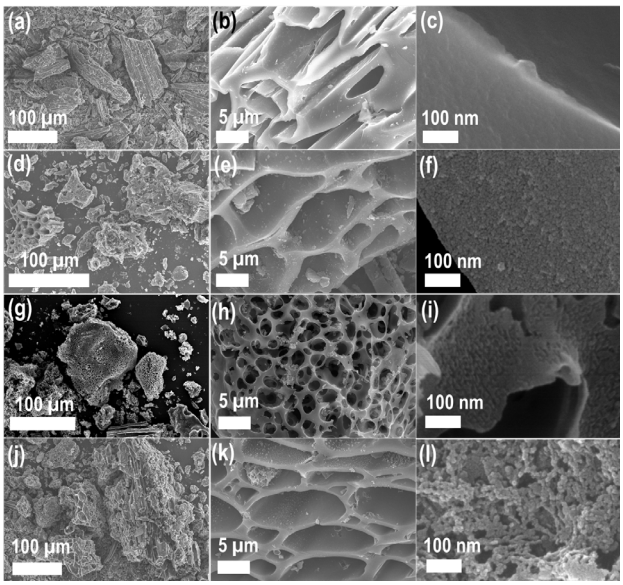
(a)
100 µm
(b)
5 µm
(c)
100 nm
(d)
100 µm
(e)
5 µm
(f)
100 nm
(g)
100 µm
(h)
5 µm
(i)
100 nm
(j)
100 µm
(k)
5 µm
(l)
100 nm

Fig. 3 (sheet 3)

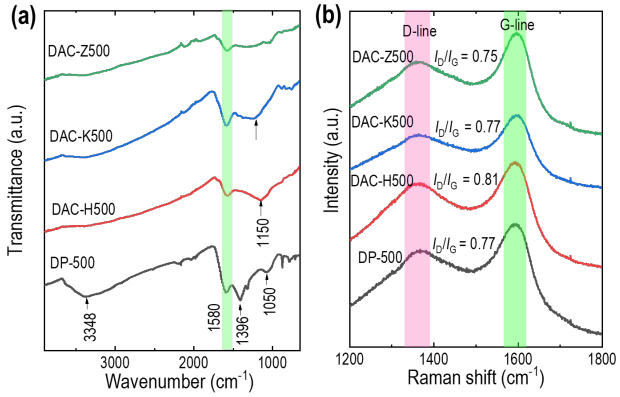
(a)
DAC-Z500
DAC-K500
DAC-H500
DP-500
3348
1580
1396
1150
1050
Transmittance (a.u.)
3000
2000
1000
Wavenumber (cm-1)
(b)
D-line
G-line
DAC-Z500
ID/IG = 0.75
DAC-K500
ID/IG = 0.77
DAC-H500
ID/IG = 0.81
DP-500
ID/IG = 0.77
Intensity (a.u.)
1200
1400
1600
1800
Raman shift (cm-1)

Fig. 4 (sheet 4)

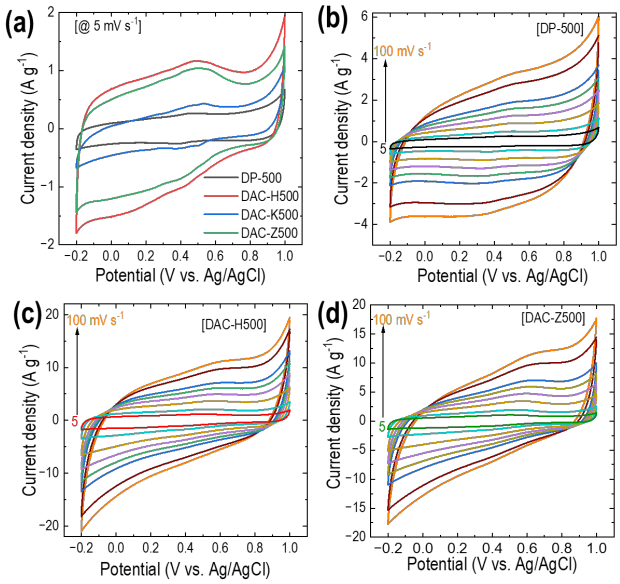
(a)
[@ 5 mV s-1]
Current density (A g-1)
Potential (V vs. Ag/AgCl)
DP-500
DAC-H500
DAC-K500
DAC-Z500
(b)
[DP-500]
100 mV s-1
5
(c)
[DAC-H500]
(d)
[DAC-Z500]

Fig.5 (sheet5)

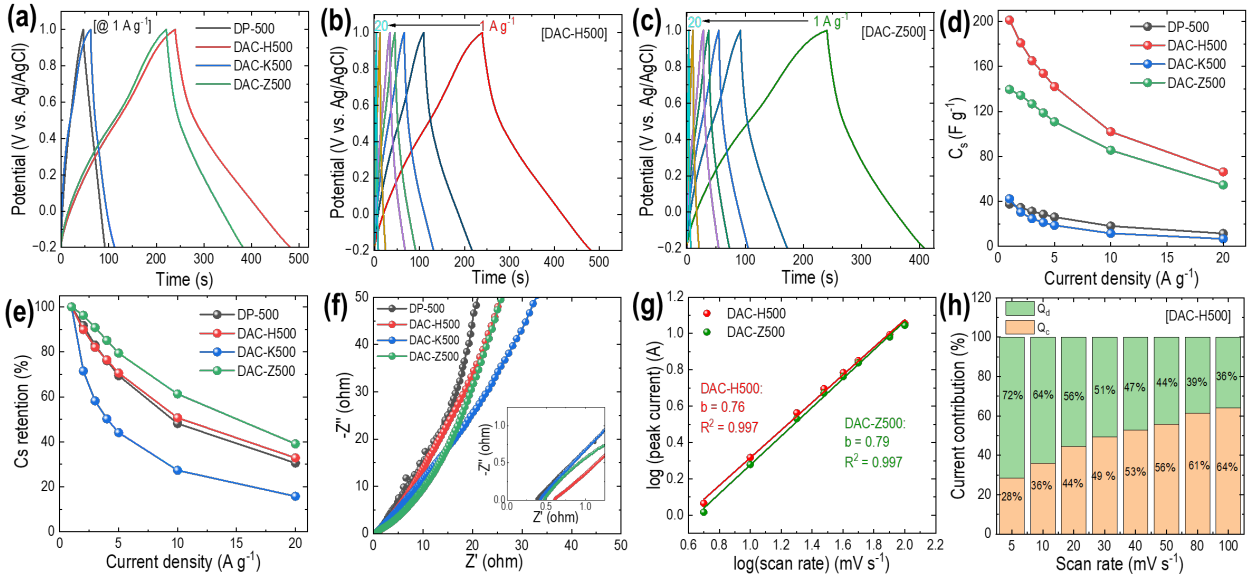
(a)
[@ 1 A g-1]
DP-500
DAC-H500
DAC-K500
DAC-Z500
Potential (V vs. Ag/AgCl)
Time (s)
(b)
20
1 A g-1
[DAC-H500]
Potential (V vs. Ag/AgCl)
Time (s)
(c)
20
1 A g-1
[DAC-Z500]
Potential (V vs. Ag/AgCl)
Time (s)
(d)
DP-500
DAC-H500
DAC-K500
DAC-Z500
Cs (F g-1)
Current density (A g-1)
(e)
DP-500
DAC-H500
DAC-K500
DAC-Z500
Cs retention (%)
Current density (A g-1)
(f)
DP-500
DAC-H500
DAC-K500
DAC-Z500
-Z'' (ohm)
Z' (ohm)
(g)
DAC-H500
DAC-Z500
DAC-H500:
b = 0.76
R2 = 0.997
DAC-Z500:
b = 0.79
R2 = 0.997
log (peak current) (A)
log(scan rate) (mV s-1)
(h)
Qd
Qc
[DAC-H500]
Current contribution (%)
72%
64%
56%
51%
47%
44%
39%
36%
28%
36%
44%
49 %
53%
56%
61%
64%
Scan rate (mV s-1)

Fig. 6 (sheet 6)

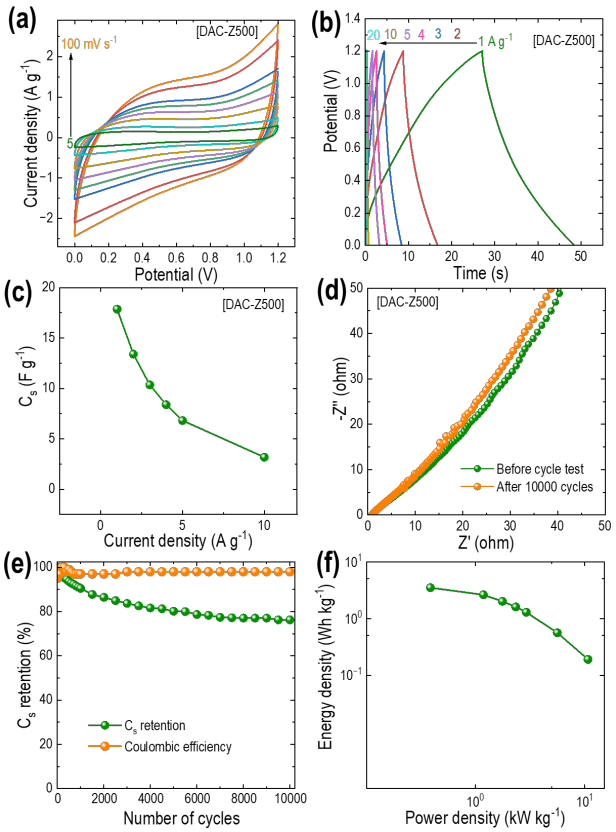

Legends of Table:

Table 1. Surface textural properties of Datiwan-derived carbon materials.

〔**Table**〕:

Table 1 (sheet 7)

Sample	*SSA* (m^2/g)	S_{micro} (m^2/g)	S_{meso} (m^2/g)	S_{BET} (m^2/g)	V_{micro} (cm^3/g)	V_{meso} (cm^3/g)	V_p (cm^3/g)	W_p (nm)	D_p (nm)
DP-500	25.5	10.6	14.9	22.6	0.025	0.028	0.053	-	3.26
DAC-H500	724.3	623.1	101.2	600.6	0.352	0.163	0.515	0.27	3.67
DAC-K500	74.8	64.9	9.9	61.3	0.061	0.042	0.103	0.70	7.90
DAC-Z500	757.9	706.1	51.8	767.9	0.360	0.093	0.453	0.27	3.80

注意） 本文中に図表を差し込むことはしないで、本文、Figure caption、 図、表の順に揃えて投稿してください